Analytical Power Fluctuation Suppression With Reconfigurable Tx Coils for Dynamic Inductive Power Transfer Systems

Huiwen Xiao, *Graduate Student Member, IEEE*, Ka Wai Eric Cheng, *Fellow, IEEE*, and Siqi Bu, *Senior Member, IEEE*

***Abstract*—This article presents a reconfigurable coil design framework for dynamic inductive power transfer systems to ensure stable and robust output characteristics while minimizing construction costs. In this article, two innovative transmitter (Tx) coil configurations are introduced: the inner and outer square (IOS) and the two half-square toroidal (THST), each designed to support flexible reconfiguration for diverse operational needs. The framework achieves this flexibility by integrating a switch-array reconfiguration mechanism with an algorithmic coil optimization methodology. The switch array facilitates varied Tx coil unit connections. Notably, antiseries connections outperform conventional single Tx coil units in suppressing output fluctuations, while forward-series connections enhance versatility, offering IOS units a wider output range and THST units improved interoperability with unipolar and bipolar receiver (Rx) coils. A numerical algorithm evaluates the dynamic mutual inductance characteristic, quantifying the impact of linear and angular misalignments on fluctuation patterns and extrema shifts. This framework not only generates a family of compensation coils by presetting fluctuation tolerance and power transfer capacity indicators for a smaller Tx coverage density but also streamlines development, outpacing traditional finite element analysis and trial-and-error methods. Both simulation and experimental results validate the framework's efficacy, demonstrating a scalable, cost-effective solution for dynamic charging applications.**

***Index Terms*—Half-square toroidal Tx coil, interoperability, output fluctuation suppression, reconfigurable Tx coils, reverse coil.**

I. Introduction

To mitigate the impediments posed by wired charging in material handling and automation, electrified on-road and railway transportation, aerial robotics, and autonomous underwater vehicles, dynamic inductive power transfer (DIPT) technology has seen notable advancements over the past two decades [1]. A typical example is the dynamic magnetic coupling structure for DIPT systems are oriented from initial power compatibility [2] to higher efficiency [3], [4], broader interoperability with diverse coil configurations [5], markedly attenuated power fluctuation [6], [7], drastically reduced same-side coil cross-coupling [8], [9]. Currently, DIPT systems are mainly divided into two main categories based on proportional lengths of the transmitter (Tx) and receiver (Rx) coils: long-track (rail-type) and segment (array-type) transmitter structures [5]. Rail-type Tx coils can provide stable power transfer to electric vehicles (EVs) in motion. However, extending Tx length results in reduced system efficiency, increased electromagnetic leakage, and worsened compatibility with static inductive power transfer systems [6]. Similar to static wireless charging units, array-type Tx coils closely correspond in dimensions to the pickup coil. These transmitters activate exclusively when coupled with the Rx coil, effectively mitigating the issues inherent to long-track transmitters. Nevertheless, segment DIPT systems inevitably experience fluctuations in output power [7]. These fluctuations arise from variations in compensation structure parameters [5], input power [10], internal battery resistance [11], and most notably, mutual inductance [12], [16], [17], [18], [19], [20], [21], [22], [23]. To address the fluctuating mutual inductance due to unpredictable effects of air gap changes and misalignments, it is important to control the front-end converter and inverter [13] or back-end converters to mitigate the coupling issue [14], as well as implement impedance matching strategies [15]. However, excessive spacing between adjacent transmitter coils to minimize cross-coupling will also lead to a predictable cyclical power drop when the receiver coil moves at the transition region [16]. Furthermore, the magnetic flux generated by adjacent transmitter coils can negate the magnetic flux of the receiving coil due to improper positioning and excitation of the Tx coils, resulting in weak coupling [12]. The degree to which this power can be stabilized strongly depends on the coupler design, particularly on the configuration and placement of Tx coils [5].

Several coil configurations and their combinations with various excitations have been explored to ensure a consistent magnetic field within the air gap between the transmitter and receiver from temporal and spatial perspectives. Temporally, fine-tuning the excitation magnitude and phase of the fixed-position transmitters suppresses the coupling variation, thereby

Received 4 January 2025; revised 20 March 2025 and 7 May 2025; accepted 30 May 2025. Date of publication 9 June 2025; date of current version 19 January 2026. This work was supported by Research Grant Council under Project 15207721. Recommended for publication by Associate Editor J. Biela. *(Corresponding author: Ka Wai Eric Cheng.)*

Huiwen Xiao and Siqi Bu are with the Department of Electrical and Electronic Engineering, The Hong Kong Polytechnic University, Hong Kong (e-mail: hui-wen.xiao@connect.polyu.hk; siqi.bu@polyu.edu.hk).

Ka Wai Eric Cheng is with the University of California, Merced, CA 95343 USA (e-mail: ericcheng@ucmerced.edu).

Color versions of one or more figures in this article are available at https://doi.org/10.1109/TPEL.2025.3577933.

Digital Object Identifier 10.1109/TPEL.2025.3577933

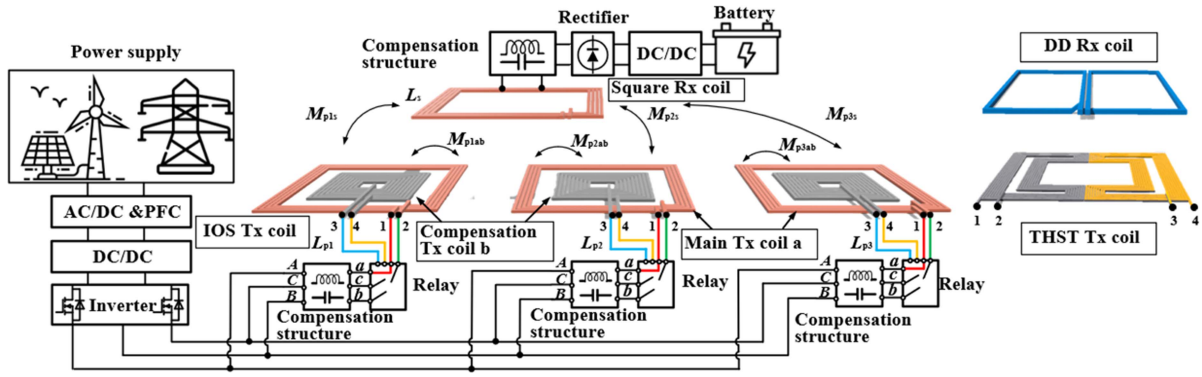

Fig. 1. Configuration of the DIPT system.

enhancing the stability of the integrated magnetic field [5], [12]. In [5], Zaheer et al. employ distinct excitation modes to evaluate field uniformity across four configurations—BPP and DDQP Tx paired with unipolar or bipolar Rx—at various displacements. A tripolar pad coupler [12], a double-layer triangular DQ Tx [17], and rectangular solenoid pads [18] are proposed to improve the coupling coefficients in the extension area by adjusting the primary current. In [19], alternately arranged three-phase Tx coils are adopted to generate a uniform magnetic field. It is more straightforward to regulate the induced voltage of Rx, with its resemblance to a multiple-phase ac motor having a traveling magnetic field. However, the phase deviation of the excited multiphase power will exacerbate the power fluctuations.

Spatially, the input currents of the Tx coils remain unchanged, thus eliminating intricate control mechanisms. Stability in mutual inductance is ensured through optimization of the geometry parameters of the Tx and Rx [20], implementation of folded, interlaced, and overlapped Tx coils [16], [21], [22], [23], and reconfigurable connectivity of coil sets [24], [25]. For instance, Geng et al. [20] present an optimally designed segmented coil pattern using a genetic algorithm to ensure a high Rx-to-Tx size ratio. Nevertheless, the limited space on the receiver side restricts the practical application. Strategies such as folded Tx [16], extended Tx [21], partially overlapped adjacent DD Tx [22], and cross-overlapped DD with quadrature Tx [23] are proposed to smooth the mutual inductance at the transition zone. However, insufficient spacing between adjacent Tx results in significant cross-coupling, thereby necessitating a complex design of the compensation network parameters. Reverse coil structure has gained attention for its intuitive design and antimisalignment capabilities [24], [25], [26], [27], [28]. However, a comprehensive design methodology and associated challenges for integrating a separate reverse coil into existing DIPT systems remain limited. In particular, the full potential of compensating coils has not yet been fully explored to extend the functionality beyond misalignment capability. By far, both temporal and spatial strategies for ensuring a consistent magnetic field have been extensively investigated, most of these designs are based on finite element analysis (FEA) software, and few designs demonstrate reconfigurability, such as adapting to multiple input power levels and accommodating both typical unipolar and bipolar receiver (Rx) coils.

To bridge the research gaps, two types of reconfigurable array-type Tx coils, i.e., inner and outer square (IOS) Tx coil units and two half-square toroidal (THST) Tx coil units, are proposed in this article. Both types exhibit reconfigurability when combined with switch arrays, as illustrated in Fig. 1. Notably, with series-opposing connections, they demonstrate superior output fluctuation suppression performance compared to the conventional single Tx coil units, particularly when the separation distances between the adjacent transmitter coil sets are large. The main contributions of this article are summarized as follows.

1. *Proposed a new segmented Tx coil design:* The THST Tx coil units, based on the IOS Tx coil, feature antiseries connections to achieve superior output fluctuation suppression at large adjacent Tx coil distances, while forward-series connection enhances interoperability with the unipolar and bipolar Rx coils in DIPT systems.
2. *Developed a switch-array configuration:* A switch-array diagram is proposed to reconfigure the connection of coil sets, enabling the full exploration of the potential of IOS Tx and THST Tx coil units.
3. *Evaluated dynamic mutual inductance characteristic:* A numerical method is developed to evaluate the spatial characteristic of mutual inductance under dynamic conditions, quantifying how lateral and angular misalignments induce fluctuations and positional shifts of its extrema, thereby enhancing coil design accuracy.
4. *Introduced an optimization framework:* An algorithmic coil optimization framework is developed to optimize compensation coil designs in DIPT systems, minimizing mutual inductance fluctuation and maximizing mutual inductance for stable and effective power transfer.

II. Proposed Reconfigurable DIPT System

A. Analysis of the LCC–LCC Compensated DIPT System

To simplify the analysis without losing generality, a double-sided *LCC*-compensated (*LCC-LCC*) DIPT system is analyzed

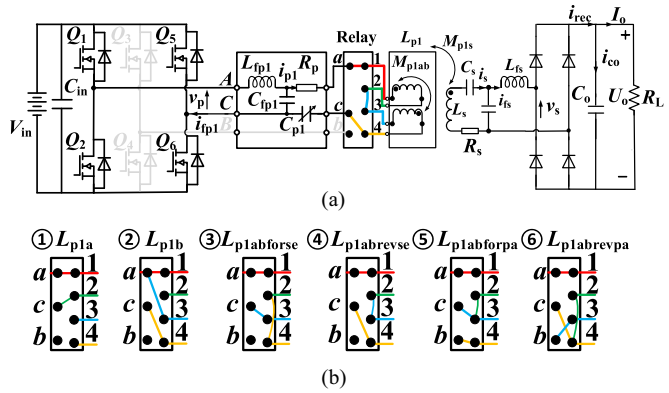

Fig. 2. (a) Schematic diagram of an *LCC-LCC* compensated IPT system with variable Tx configuration. (b) Relay connections diagram for reconfigurable Tx coils in the DIPT system.

TABLE I
PARAMETERS OF VARIOUS CONNECTIONS OF MAIN AND COMPENSATION TRANSMITTER COILS

Symbol	Type	L_{p1} (μH)	M_{p1s} (μH)
L_{p1a}		L_{p1a} =43.04	M_{p1as} =8.09
L_{p1b}		L_{p1b} =14.72	M_{p1bs} =5.94
$L_{p1abforse}$		$L_{p1a}+L_{p1b}+2M_{p1ab}$=79.6	$M_{p1abforses}$ =19.75
$L_{p1abrevse}$		$L_{p1a}+L_{p1b}$-2M_{p1ab}= 34.28	$M_{p1abrevse}$ =7.8
$L_{p1abforpa}$		$\frac{L_{p1a}L_{p1b}-M_{p1ab}^2}{L_{p1a}+L_{p1b}-2M_{p1ab}}$ =13.68	$M_{p1abforpa}$ =6.45
$L_{p1abrevpa}$		$\frac{L_{p1a}L_{p1b}-M_{p1ab}^2}{L_{p1a}+L_{p1b}+2M_{p1ab}}$ =5.82	$M_{p1abrevpa}$ =0.2975

in this article. The circuit diagram of an *LCC-LCC* compensated IPT system, along with the corresponding relay connections to achieve reconfigurability, is plotted as shown in Fig. 2. Here, L_{px} and L_{fpx} are the self and compensation inductances of the xth Tx coils. L_{pxa} and L_{pxb} are the self-inductances of the main and compensation Tx coils. L_s and L_{fs} are the self and compensation inductances of the Rx coils. M_{pxs} is the mutual inductance between the coupled Tx and Rx coils, respectively. M_{pxab} is the mutual inductance between the main and compensation Tx coils. C_{px}, C_{fpx}, C_s, and C_{fs} are the compensation capacitances. R_{px} and R_s are the equivalent series resistances (ESRs) of the coils. C_o is the filter capacitance. R_{eqL} is the equivalent load resistance of the diode-bridge rectifier, filter capacitor, and resistive load R_L (i.e., $R_{eqL} = 8R_L/\pi^2$) [29]. V_{in} is the input dc voltage. I_o and U_o are the output dc current and voltage. v_{px} and i_{fpx} are the input voltage and current of the Tx resonators. v_s and i_{fs} are the Rx resonator voltage and currents. i_{px} and i_s are the currents of the Tx and Rx coils. i_{rec} and i_{co} are the rectified current and filter capacitor current. ω_s and ω_o are the operating and resonant angular frequencies.

According to Kirchhoff's law and the Fourier analysis, the fundamental components of v_{p1}, i_{p1}, i_{fp1}, and i_{fs} with ω_s controlled at ω_o can be obtained as

$$v_{p1}(t) = \frac{4V_{in}\cos(\alpha/2)}{\pi}\sin(\omega_s t) \tag{1}$$

$$i_{p1}(t) = \frac{4V_{in}\cos(\alpha/2)}{\pi\omega_s L_{fpl}}\sin\left(\omega_s t - \frac{\pi}{2}\right) \tag{2}$$

$$i_{fp1}(t) = \frac{4V_{in}M_{p1s}{}^2R_{eqL}\cos(\alpha/2)}{\pi\omega_s{}^2L_{fpl}{}^2L_{fs}{}^2}\sin(\omega_s t) \tag{3}$$

$$i_{fs}(t) = \frac{4V_{in}M_{p1s}\cos(\alpha/2)}{\pi\omega_s L_{fpl}L_{fs}}\sin\left(\omega_s t - \frac{\pi}{2}\right) \tag{4}$$

where the circuit parameters are designed to satisfy

$$\begin{cases}\omega_o L_{fpl} = 1/\omega_o C_{fpl} = \omega_o L_p - 1/\omega_o C_p \\ \omega_o L_{fs} = 1/\omega_o C_{fs} = \omega_o L_s - 1/\omega_o C_s\end{cases}. \tag{5}$$

Here, α is the phase shift angle of the diagonal power switches of the single-phase transmitter-side inverter. Apparently, the output current of the receiver can be controlled by the phase shift angle α and operating frequency f_s (i.e., $f_s = \omega_s/2\pi$), but is also affected by the system parameters, including L_{fp1}, L_{fs}, C_o, M_{p1s}, and V_{in}. Based on (1) and (2), the *LCC-LCC* compensation network maintains the stability of the current in the Tx coil (i.e., i_{p1}), regardless of the variations in coupling conditions and load. This compensation network also exhibits constant current source output characteristics, irrespective of fluctuations in load, and attains a zero-phase angle for the DIPT system based on (1), (3), and (4). Therefore, disregarding the parameter drift and power supply fluctuations [10], [30], the output current i_{fs} of the receiver resonator is monotonically changed with the mutual inductance between coupled transmitter and receiver coils (i.e., M_{p1s}). Thus, maintaining consistent M_{p1s} through optimally designed coupling coils, irrespective of the receiver's position, ensures stable output power.

B. Coupling and Output Characteristic

To exhibit the coupling performance of the reconfigurable Tx coils shown in Fig. 2, the measured parameters for six configurations of IOS Tx coils are given in Table I. These configurations include single coil *a*, single coil *b*, and combinations of coil *a* and *b* in forward-series, reverse-series, forward-parallel, and reverse-parallel connections. It is worth noting that Tx coils connected in parallel and antiparallel are excluded due to minimal coupling performance for the DIPT system in this study, as shown in Table I. Consequently, the three-phase inverter can be simplified to a single-phase inverter. Installing two single-pole double-throw switches at nodes 3 and 4 enables the implementation of both forward and reverse series configurations.

To exhibit the output range across distinct configurations, I_{fs}-α curves and I_{fs}-f_s curves for these configurations are plotted, as shown in Fig. 3. It is evident that Tx coils with different connections exhibit varying mutual coupling capacities, allowing for a broader output range by altering connections of the compensation and main Tx coils, as compared to solely adjusting the control variables (f_s and α), as described in (4) and depicted in Table I and Fig. 3. As illustrated in Fig. 3(a) and (b), the forward-series connection exhibits the broadest output range for I_{fs}, while also demonstrating the greatest sensitivity

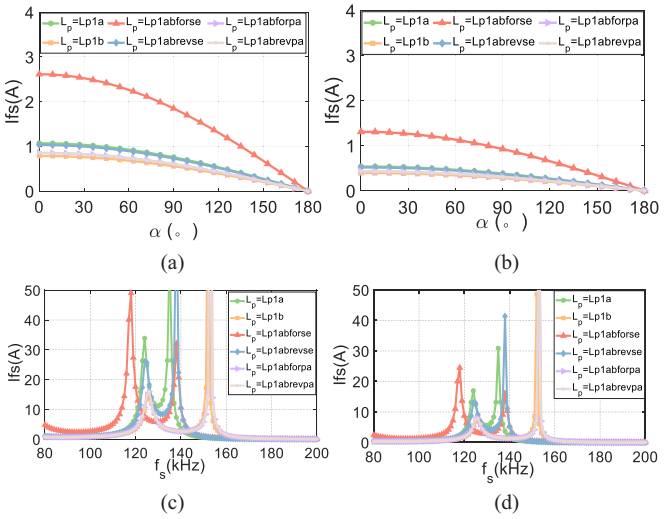

Fig. 3. Curves of (a) $I_{\rm fs}$-α with $V_{\rm in} = 40$ V, (b) $I_{\rm fs}$-α with $V_{\rm in} = 20$ V, (c) $I_{\rm fs}$-f_s with $V_{\rm in} = 40$ V, and (d) $I_{\rm fs}$- $f_{\rm s}$ with $V_{\rm in} = 20$ V of the reconfigurable DIPT system.

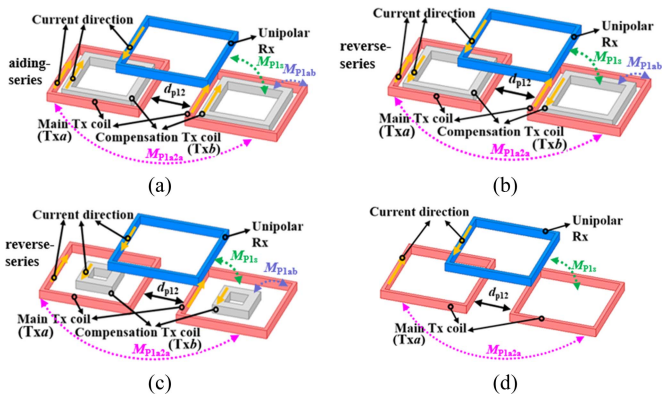

Fig. 4. Coil structure of the coupler displaying (a) Tx series-aiding connection. (b) Tx series-opposing connection with $M_{\rm pab} = 4.77$ μH and $L_{\rm pb} = 38.4$ μH. (c) Tx series-opposing connection with $M_{\rm pab} = 9.68$ μH and $L_{\rm pb} = 11.4$ μH. (d) Tx without compensation coil.

of $I_{\rm fs}$ with respect to α among within the six configurations. A fixed configuration of the Tx coil may result in undesirable output when the input voltage fluctuates due to variations in user power demand and the penetration of renewable energy sources [10], [30]. Besides, the output range for a single Tx coil is constrained even if control variables (f_s and α) are adjusted, as shown in Fig. 3. Therefore, to ensure a wider output, this article introduces the reconfigurable IOS Tx coil units, thereby achieving greater flexibility and robustness.

C. Cross-Coupling Characteristic

Fig. 5(a) illustrates the relationship between the cross-coupling ($M_{\rm p1a2a}$) of two neighboring main Tx coil a and the separation distance $d_{\rm p12}$ for various IOS Tx coil configurations depicted in Fig. 4. Clearly, for all the configurations shown in Fig. 4, MATLAB's knee point function is adopted to identify the optimal separation distance, which is found to be 50 mm

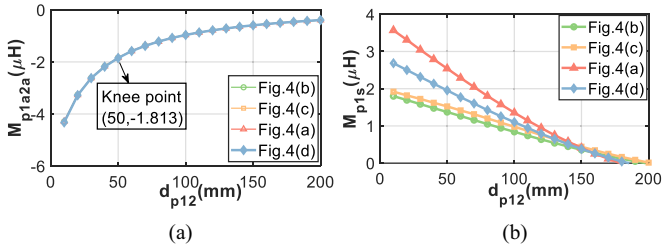

Fig. 5. (a) $M_{\rm p1a2a}$- $d_{\rm p12}$ and (b) $M_{\rm p1s}$- $d_{\rm p12}$ curves of the DIPT system with different configurations of the Tx coils.

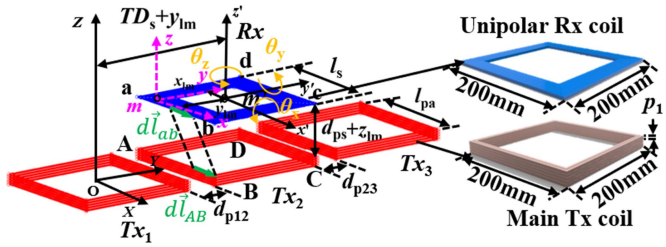

Fig. 6. Schematic diagram of the DIPT system.

as reported in Fig. 5(a). This analysis is based on FEM-derived cross-coupling data.

To exhibit the effect of the spacing between adjacent Tx coils on mutual inductance, with a unipolar Rx coil positioned precisely at the midpoint above these coils, the relationship between the $d_{\rm p12}$ and $M_{\rm p1s}$ based on configurations in Fig. 4 is plotted in Fig. 5(b). It can be observed from Fig. 5(b) that, compared to $M_{\rm p1s}$ at $d_{\rm p12} = 0$ mm, the reduction in $M_{\rm p1s}$ at $d_{\rm p12} = 50$ mm is approximately 31.8% for Tx coils without compensation coils (Txb), 33.68% for Tx coils with the series-aiding connection, and 24.3% for Tx coils with the series-opposing connection. This indicates that the series-opposing connected Tx coils exhibit the least sensitivity to the separation gap. In addition, different turns and geometries of the compensation coil b as shown in Fig. 4(b) and (c), indicated by different $M_{\rm p1ab}$ and $L_{\rm p1b}$ values, result in a similar mutual inductance at a given separation distance between Tx coils. Therefore, a well-designed compensation coil can reduce the sensitivity to the separation gap. Comparative studies of different Txb that result in similar $M_{\rm p1s}$ will be investigated in Section IV.

III. Analysis of the Fluctuation of the $M_{\rm PS}$

A. Proposed Numerical Algorithm

To analyze the fluctuation of mutual inductance $M_{\rm pxas}$ between the main Tx (Txa) and Rx coils within the DIPT system, the cumulative mutual inductance $M_{\rm passum}$ in the presence of linear and angular misalignments along the y-axis is examined utilizing the Neumann formula, as depicted in Fig. 6. The absolute difference in mutual inductance between the peak mutual inductance ($M_{\rm pasmax}$) and the lowest mutual inductance ($M_{\rm pasmin}$)—termed the mutual inductance drop $\Delta M_{\rm pas}$—can be

calculated. A larger ΔM_{pas} denotes a more significant discrepancy between the aligned and misaligned positions, thereby highlighting the potential impact on output power stability based on (4).

The mutual inductance for arbitrary line segments (i.e., *AB* and *ab*) is

$$M_{AB\_ab} = \frac{\mu_0}{4\pi} \oint \oint \frac{d\vec{l}_{AB}.d\vec{l}_{ab}}{r}. \tag{6}$$

Here, the vacuum magnetic permeability μ_0 is $4\pi*10^{-7}$ (H/m). $d\vec{l}_{AB}$ and $d\vec{l}_{ab}$ are the vector differential length elements. *r* is the distance between the two elements. The mutual inductance for arbitrary line segments with linear and angular misalignment based on the partial inductance method [31] can be calculated as

$$M_{AikBik\_ajhbjh} = \frac{\mu_0}{4\pi} \int_{x_{ajh}}^{x_{bjh}} \int_{x_{Aik}}^{x_{Bik}} \frac{1 + K_1K_2 + K_3K_4}{\sqrt{K_5^2 + K_6^2 + K_7^2}} dx_{AikBik} dx_{ajhbjh}. \tag{7}$$

Based on the coordinates of point $A_{\text{ik}}(x_{\text{Aik}}, y_{\text{Aik}}, z_{\text{Aik}})$, $B_{\text{ik}}(x_{\text{Bik}}, y_{\text{Bik}}, z_{\text{Bik}})$, $a_{\text{jh}}(x_{\text{ajh}}, y_{\text{ajh}}, z_{\text{ajh}})$, $b_{\text{jh}}(x_{\text{bjh}}, y_{\text{bjh}}, z_{\text{bjh}})$, and the direction vector x_{AikBik} and x_{ajhbjh}, the coefficients are defined as

$$\begin{aligned}
K_1 &= \frac{y_{Bik} - y_{Aik}}{x_{Bik} - x_{Aik}}, K_2 = \frac{y_{bjh} - y_{ajh}}{x_{bjh} - x_{ajh}}, K_3 = \frac{z_{Bik} - z_{Aik}}{x_{Bik} - x_{Aik}}, \\
K_4 &= \frac{z_{bjh} - z_{ajh}}{x_{bjh} - x_{ajh}}, K_5 = x_{ajhbjh} - x_{AikBik}, \\
K_6 &= K_1 (x_{AikBik} - x_{Aik}) - K_2 (x_{ajhbjh} - x_{ajh}) \\
&\quad + y_{Bik} - y_{ajh}, \\
K_7 &= K_3 (x_{AikBik} - x_{Aik}) - K_4 (x_{ajhbjh} - x_{ajh}) \\
&\quad + z_{Aik} - z_{ajh}.
\end{aligned} \tag{8}$$

For square coils, as shown in Fig. 6, the coordinates of vertices (A_{ik}, B_{ik}, C_{ik}, D_{ik}) of the *i*th turn in the *k*th layer for Tx coils can be defined as follows:

$$\begin{aligned}
A_{ik} &= [C_{px} + l_p/2 - xy_{pki}, C_{py} + l_p/2 - xy_{pki}, C_{pz} - z_{pk}] \\
B_{ik} &= [C_{px} - l_p/2 - xy_{pki}, C_{py} + l_p/2 - xy_{pki}, C_{pz} - z_{pk}] \\
C_{ik} &= [C_{px} - l_p/2 - xy_{pki}, C_{py} - l_p/2 - xy_{pki}, C_{pz} - z_{pk}] \\
D_{ik} &= [C_{px} + l_p/2 - xy_{pki}, C_{py} - l_p/2 - xy_{pki}, C_{pz} - z_{pk}].
\end{aligned} \tag{9}$$

Here, both the *x*-axis and *y*-axis offset of each coil turn (i.e., xy_{pki}) is $n_{pki} * p_1$, while the *z*-axis offset of each coil turn (i.e., z_{pk}) is $n_{pk} * p_1$. l_p and p_1 are the side length and pitch of the coil, where the center coordinates of the main Tx and Rx coils are as

$$\text{C}_p = [C_{px}, C_{py}, C_{pz}] \tag{10.1}$$

$$\text{C}_s = [x_{lm}, \text{TD}_s + y_{lm}, d_{ps} + z_{lm}]. \tag{10.2}$$

TD_s is the traveling distance of the Rx coil along the *y*-axis, referring to the distance between the centers of the first Tx and Rx coils. d_{ps} is the air gap between the Tx and Rx. Linear misalignments x_{lm}, y_{lm}, and z_{lm} pertain to deviations of the Rx coil along the *x*, *y*, and *z*-axis. Angular misalignments θ_x, θ_y, and θ_z signify rotations of the Rx coil around the *x*, *y*, and *z*-axis, respectively. The vertices of Rx coils (a_{jh}, b_{jh}, c_{jh}, d_{jh}) with misalignments can be described as

$$[a_{ik}; b_{ik}; c_{ik}; d_{ik}] = [\theta_{am}] ([a_{ik}; b_{ik}; c_{ik}; d_{ik}] - \text{C}_s) + \text{C}_s \tag{11.1}$$

where the matrix of angular misalignment is

$$[\theta_{am}] = \begin{bmatrix} \theta_{am11} & \theta_{am12} & \theta_{am13} \\ \theta_{am21} & \theta_{am22} & \theta_{am23} \\ \theta_{am31} & \theta_{am32} & \theta_{am33} \end{bmatrix} \tag{11.2}$$

$$\begin{aligned}
\theta_{am11} &= \cos\theta_z \cos\theta_y \\
\theta_{am12} &= \cos\theta_z \sin\theta_y \sin\theta_x - \sin\theta_z \cos\theta_x \\
\theta_{am13} &= \cos\theta_z \sin\theta_y \cos\theta_x + \sin\theta_z \sin\theta_x \\
\theta_{am21} &= \sin\theta_z \cos\theta_y \\
\theta_{am22} &= \sin\theta_z \sin\theta_y \sin\theta_x + \cos\theta_z \cos\theta_x, \\
\theta_{am23} &= \sin\theta_z \sin\theta_y \cos\theta_x - \cos\theta_z \sin\theta_x, \\
\theta_{am31} &= -\sin\theta_y \\
\theta_{am32} &= \cos\theta_y \sin\theta_x \\
\theta_{am33} &= \cos\theta_y \cos\theta_x.
\end{aligned} \tag{11.3}$$

The mutual inductance of the main Tx and Rx coils can be described as

$$M_{\text{pas}} = \sum_{k=1}^{n_{\text{pak}}} \sum_{h=1}^{1} \sum_{i=1}^{n_{\text{paki}}} \sum_{j=1}^{N_S} M_{AikBik\_ajhbjh}. \tag{12}$$

To identify the position of M_{pasmax} and M_{pasmin} (TD_{smax} and TD_{smin}), the derivative of the M_{passum} ($M_{\text{passum}} = \sum_{x=1}^{6} M_{\text{pxas}}$) with respect to TD_s is examined to locate the extreme point (i.e., M_{pasmax} and M_{pasmin}), a numerical approach using the finite difference method approximates this derivative as

$$\frac{\partial (M_{\text{passum}})}{\partial (\text{TD}_s)} \approx \frac{((M_{\text{passum}}) |\text{TD}_s + \Delta\text{TD}_s) - ((M_{\text{passum}}) |\text{TD}_s)}{\Delta\text{TD}_s} \tag{13}$$

where ΔTD_s is a step increment of TD_s. By iterating this calculation over a range of TD_s values, M_{pasmax} is identified when the derivative transitions from positive to negative, whereas M_{pasmin} occurs when the derivative changes from negative to positive. The zero-crossing point of M_{passum} can be found to check the sign of M_{passum}. Typically, M_{pasmax} occurs when the Rx is centered over the Tx, mathematically expressed as $\text{TD}_{\text{smax}} = d_{\text{p12}} + l_{\text{pa}}$; M_{pasmin} is observed at $\text{TD}_{\text{smin}} = 3*(d_{\text{p12}} + l_{\text{pa}})/2$. However, for an Rx coil with θ_x, TD_{smax} and TD_{smin} deviate from their typical locations. Fig. 7 presents a comparison of these values as obtained via FEA software and the proposed numerical approach under θ_x misalignment. Obviously, the results prove the effectiveness of the proposed numerical approach.

The drop ΔM_{pas} is

$$\Delta M_{\text{pas}} = M_{\text{pasmax}} - M_{\text{pasmin}}. \tag{14}$$

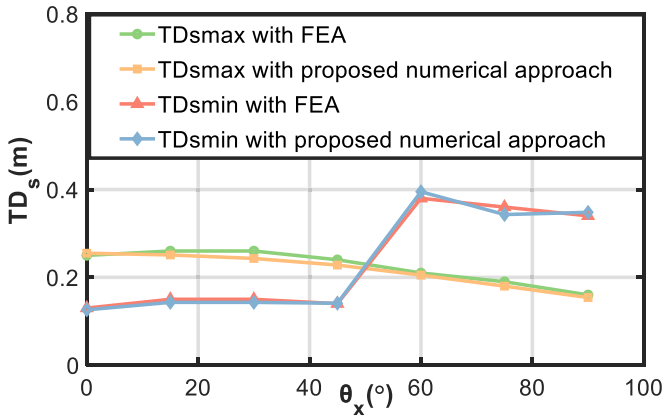

Fig. 7. Curves of TD_{smax}- θ_x and TD_{smin}- θ_x for the DIPT system.

Apparently, ΔM_{pas} is affected by geometries, sizes, pitches, turns of Tx and Rx coils, separation distances of Tx coils, Rx position, and misalignments, especially angular misalignments around the x-axis (θ_x). It is worth noting that the conventional design reference at the typical positions [32] does not apply to the system with θ_x misalignments. Furthermore, for specific power levels of DIPT systems, l_{pa}, l_s, n_{pak}, n_{paki}, N_s , and p_1 are determined. The air gap d_{ps}, linear and angular misalignment ($x_{lm}, y_{lm}, z_{lm}, \theta_x, \theta_y$, and θ_z) depend on practical conditions. The only controllable design parameter is d_{p12} when TD_s changes. Thus, the flexibility of a single main Tx coil in the DIPT system is inherently constrained.

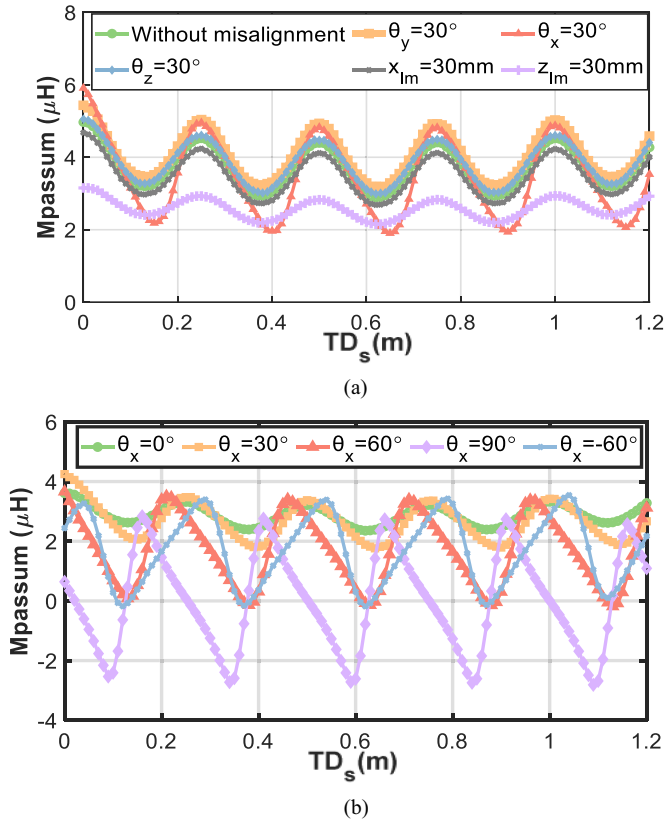

Fig. 8. Curves of M_{passum} (a) with linear and angular misalignments and (b) with angular misalignment of the x-axis for the DIPT system.

B. Simulation Verification

To exhibit the fluctuation of M_{passum} more explicitly, Rx coil with misalignments is conducted on the FEA software, Ansys Maxwell. All design configurations employ an identical planar spiral square Rx coil with coil dimensions set to $l_s = 200$ mm, and winding turns $N_s = 12$. The referenced tightly-wound, five-layer (i.e., $n_{pak} = 5$) coaxial Tx coils also have dimensions of $l_{pa} = 200$ mm, with each layer n_{paki} comprising 2 turns, as shown in Fig. 6. d_{ps} and d_{p12} are set as 80 and 50 mm. As illustrated in Fig. 8(a), both M_{passum} with and without misalignments exhibit nonuniformity along the y-axis. M_{passum} without misalignments experiences periodic oscillations of 1.5 μH at intervals equal to ($l_{pa} + d_{p12}$). For angular misalignments, M_{passum} with $\theta_x = 30°$ presents the most pronounced cyclic variations of 58.3%, while that with $\theta_z = 30°$ results in similar performance with M_{passum} without any misalignments. For linear misalignments, M_{passum} with $z_{lm} = 30$ mm demonstrates the minimal variations of 24.1%, though it also corresponds to the greatest reduction in M_{passum}. For all scenarios except for M_{passum} with $\theta_x = 30°$, M_{pasmax} occurs when the Rx coil is optimally aligned (i.e., $TD_{smax} = 250$ mm) regardless of any linear or angular misalignments; M_{pasmin} is observed when the Rx coil is positioned at the midpoint of the gap (i.e., $TD_{smin} = 375$ mm).

To further illustrate the effect of θ_x on the TD_{smax} and TD_{smin}, simulations are also conducted on the nominal DIPT system with $d_{ps} = 121$ mm, as depicted in Fig. 8(b). It can be observed from Fig. 8(b) that the rotation of the Rx coil along the x-axis, whether clockwise or counterclockwise, results in inconsistencies in the positional offsets of TD_{smax} and TD_{smin}. By comparing the curves of M_{passum} with $\theta_x = 60°$ and $\theta_x = -60°$, it is intuitive to find out that M_{pasmax} and M_{pasmin} are similar but the positional offsets for TD_{smax} and TD_{smin} are different. The positional offsets for TD_{smax} are decreased and those for TD_{smin} are increased compared to the baseline condition without rotation (i.e., $TD_{smax} = 250$ mm and $TD_{smin} = 375$ mm) when the Rx coil rotates counterclockwise. This phenomenon is more serious as θ_x increases. Notably, the former positions of M_{pasmax} and M_{pasmin} (i.e., $TD_{smax} = 250$ mm and $TD_{smin} = 375$ mm) have transitioned to points of zero mutual inductance, resulting in a complete absence of power output based on (4). At these specific positions, the mutual inductance reverses, thereby doubling its fluctuation frequency as the Rx coil travels a distance equal to ($l_{pa} + d_{p12}$). For one-to-one coupled coils with symmetrical geometry, identical angular misalignments at the x and y-axis (θ_x and θ_y) produce similar changes in M_{pas}. However, θ_x exacerbates the nonuniformity of M_{pas} along the Rx coil's traveling direction (i.e., y-axis) by amplifying the cyclic variations and shifting the positions of TD_{smax} and TD_{smin}. Consequently, the asymmetry in the distribution of M_{passum} introduced by θ_x , further complicates the system's performance and the design of compensation coils.

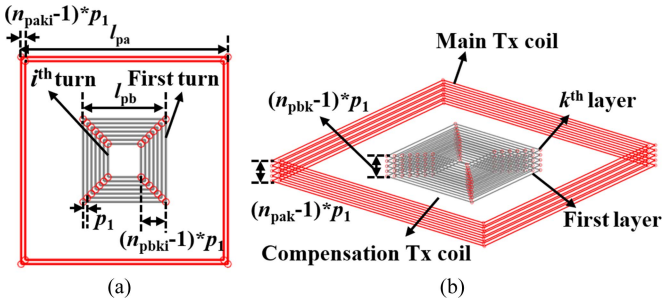

Fig. 9. (a) Top view and (b) 3-D view of the IOS Tx coils for the DIPT system.

IV. Design of the Compensation Tx Coil

A. Optimization Methodology

To address the limited misalignment capacity of a single Tx coil, an additional coaxial compensation Tx coil is incorporated to mitigate fluctuations and enhance system adaptability, namely IOS Tx coil units, as depicted in Fig. 9. As previously mentioned in Figs. 3 and 5(b), Tx coils with the series-aiding connection presents wider output than that with series-opposing connection, whereas Tx coils with series-opposing connection exhibit smaller sensitivity to the separation gap d_{p12}. Therefore, the reverse-series coil Tx*b* is adopted to reduce the fluctuation of M_{passum}. Similarly, M_{pbsmax} and M_{pbsmin} can be deduced based on (12) and (13). When the current flowing through the Tx*b* is in opposition to that flowing through the Tx*a*, the mutual inductance drops of the Tx (i.e., ΔM_{ps}) is

$$\Delta M_{ps} = M_{psmax} - M_{psmin} \tag{15}$$

where M_{psmax} and M_{psmin} are as

$$\begin{aligned} M_{psmax} &= M_{pasmax} - M_{pbsmax} \\ M_{psmin} &= M_{pasmin} - M_{pbsmin}. \end{aligned} \tag{16}$$

The objective of optimizing the Tx*b* design in a DIPT system is to minimize ΔM_{ps} and maximize M_{ps}, thereby ensuring more consistent and efficient power transfer in DIPT systems. As depicted in Fig. 10, the design flowchart for determining the parameters of the Tx*b* involves fine-tuning several key variables: outer length, l_{pb}, layers n_{pbk}, and turns at the kth layer of the compensation coil n_{pbki}. Their optimal counterparts are denoted as l_{pbo}, n_{pbko}, and n_{pbkio}, respectively. The optimal M_{p2smax} is indicated by $M_{p2smaxo}$. The process begins by initializing the Tx*a* and Rx coil parameters, followed by establishing misalignment parameters and separation distances to account for potential positional deviations. Initial compensation coil parameters are set to their maximum designed values, where $l_{pb} = l_{pa} - 2*p_1$, $n_{pbk} = n_{pak}$, and $n_{pbki} = l_{pb}/(2*p_1)$. An iterative process then calculates M_{psmax}, M_{psmin}, and ΔM_{ps} based on (12)–(16). The design's performance is evaluated using the ratio $\delta = \Delta M_{ps}/(M_{psmax} + M_{psmin})$, which represents the standard deviation of mutual inductance. A smaller value indicates better uniformity. This ratio is compared to a threshold δth to determine acceptability. In addition, the mutual inductance reduction indicator σ (i.e., $\sigma = M_{psmax}/M_{pasmax}$) is assessed

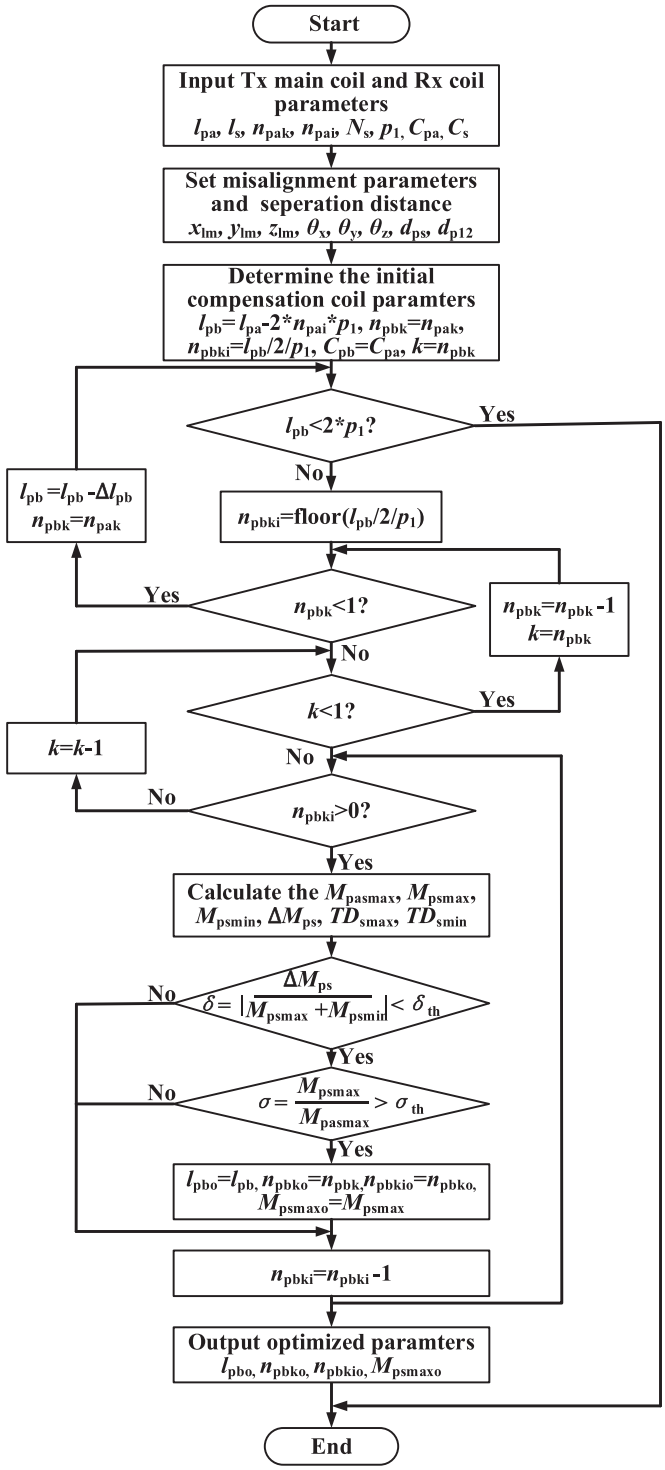

Fig. 10. Flowchart of the algorithm to determine n_{pbko}, n_{pbkio}, l_{pbo}, and $M_{p2smaxo}$.

to ensure sufficient power transfer capacity. Here, M_{psmax} is set to no less than σth of the M_{pasmax} for the given outer length. If it does, the optimal parameters are updated. If not, the number of turns in the highest layer is sequentially reduced, followed by a reduction in the number of layers. This process continues until the optimal parameters n_{pbko} and n_{pbkio} for the given

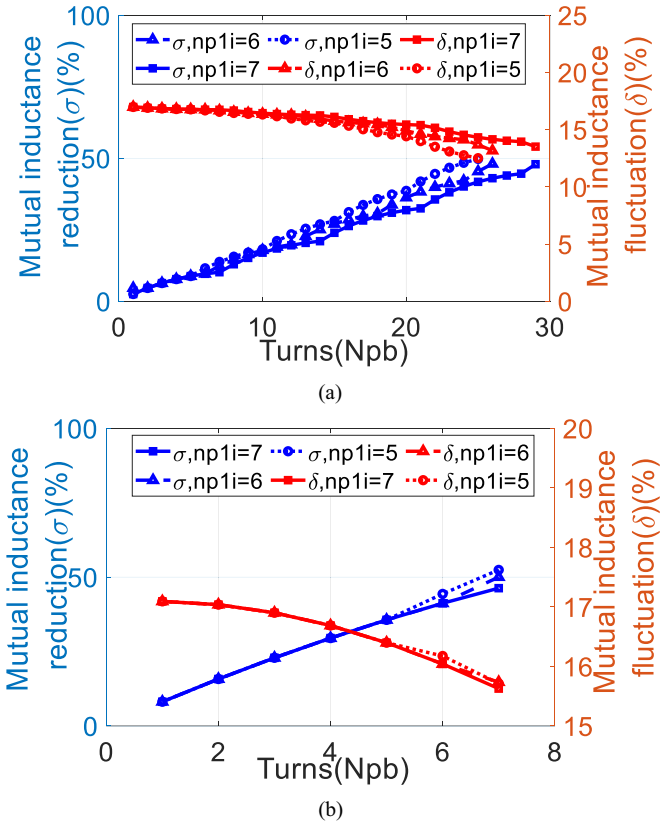

Fig. 11. Curves of δ- $N_{\rm pb}$ and σ- $N_{\rm pb}$ (a) with $l_{\rm pb} = 90$ mm and (b) with $l_{\rm pb} = 180$ mm.

$l_{\rm pbo}$ are achieved. It is worth noting that, while a sparse-coil or fractional-turn design could further reduce fluctuations, this article employs a full-turn, densely wound configuration to simplify manufacturing while balancing the tradeoff between copper loss and fluctuation.

To showcase the misalignment and power transfer capacity, the σ - $N_{\rm pb}$ and δ - $N_{\rm pb}$ relationships for various given outer lengths ($l_{\rm pb}$) and first-layer turns ($n_{\rm pb1i}$) are plotted based on the design flowchart, as shown in Fig. 11. Apparently, the reverse compensation coil mitigates mutual inductance fluctuation by decreasing the power transfer capability. In addition, the optimization program identifies several combinations that meet the specified conditions (i.e., δth $= 0.2$ and σth $= 0.5$), broadly classified into two categories: one with a small number of turns $N_{\rm pb}$ (i.e., $N_{\rm pb} = n_{\rm pbk} * n_{\rm pbki}$) and a large $l_{\rm pb}$, and the other with a large $N_{\rm pb}$ and a small $l_{\rm pb}$, as depicted in Fig. 4(b) and (c). This phenomenon aligns with the basic formula for the magnetic field, where the magnetic field generated by Txb ($B_{\rm pb}$) is approximately proportional to the number of turns divided by the coil's circumference ($B_{pb} \propto N_{pb}/l_b$). An intriguing design for Tx coils with series-opposing connection emerges when the number of turns in the antiseries coil (Txb) equals that of the main coil (Txa) (i.e., $n_{\rm pbk} * n_{\rm pbki} = n_{\rm pak} * n_{\rm paki}$). In this scenario, the IOS Tx coil depicted in Fig. 9 can be converted into THST coils, as shown in Fig. 12.

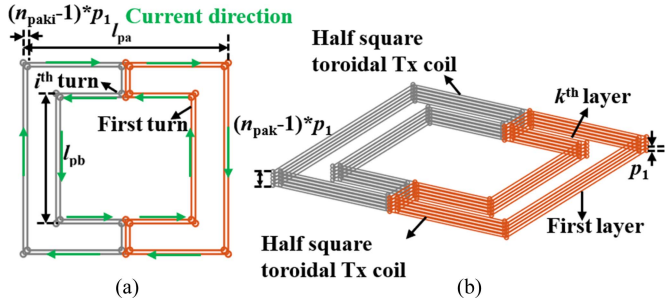

Fig. 12. (a) Top view and (b) 3-D view of the proposed THST Tx coils for the DIPT system.

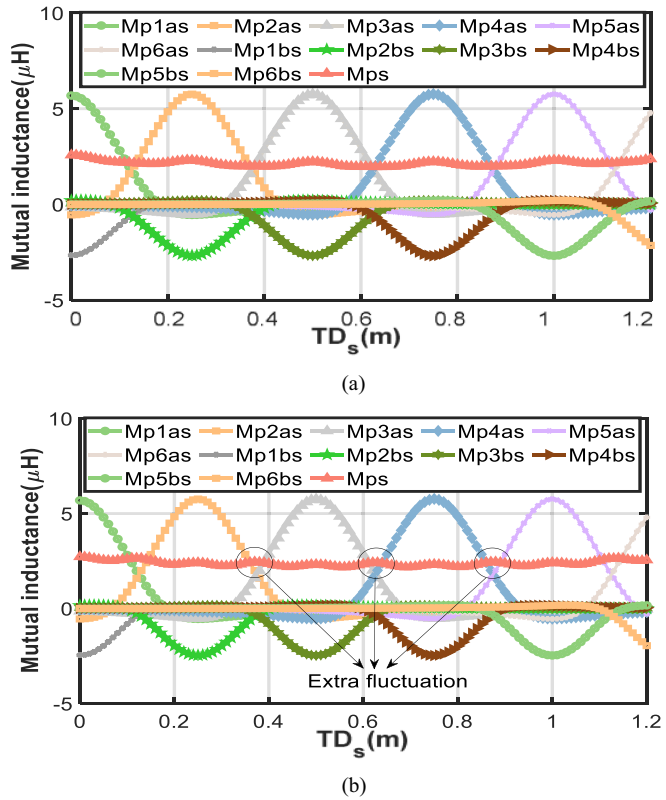

Fig. 13. Curves of $M_{\rm pxas}$- TD$_s$, $M_{\rm pxbs}$- TD$_s$, and $M_{\rm ps}$- TD$_s$ with (a) $M_{\rm pab} = 8.28$ μH and (b) $M_{\rm pab} = 5.55$ μH for the DIPT system.

B. Simulation Verification

To demonstrate the effectiveness of the proposed compensation coil design algorithm, simulations are conducted on the nominal DIPT system. Fig. 13 presents the curves of $M_{\rm pxas}$, $M_{\rm pxbs}$, and $M_{\rm ps}$ for the IOS Tx coils in series-opposing connection Tx with $M_{\rm pab} = 5.55$ μH and $M_{\rm pab} = 8.28$ μH, as depicted in Fig. 4(b) and (c) for the DIPT system. The parameters for the Txb coil in Fig. 4(b) are $l_{\rm pb} = 0.18$m and $N_{\rm pb} = 8$ turns, while those in Fig. 4(c) are $l_{\rm pb} = 0.09$ m and $N_{\rm pb} = 21$ turns. Fig. 13(a) shows $M_{\rm psmax}$ and $M_{\rm psmin}$ values of 2.23 μH and 1.99 μH, respectively. These values are slightly smaller than those presented in Fig. 13(b), which are 2.41 μH and 2.18 μH. It is evident that $\Delta M_{\rm ps}$ in both Fig. 13(a) and (b) are smaller than that without

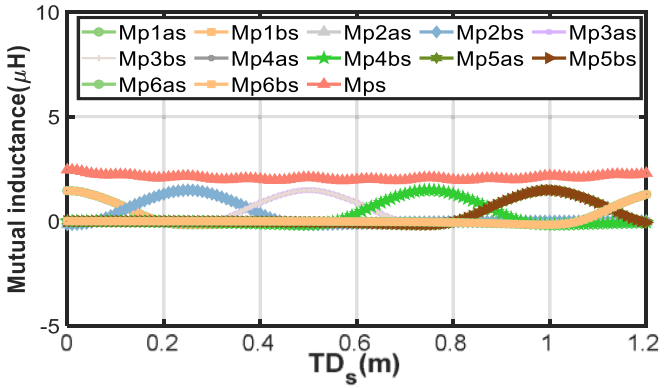

Fig. 14. Curves of M_{pxas}- TD$_s$, M_{pxbs}- TD$_s$, and M_{ps}- TD$_s$ of the proposed THST coils design for the DIPT system.

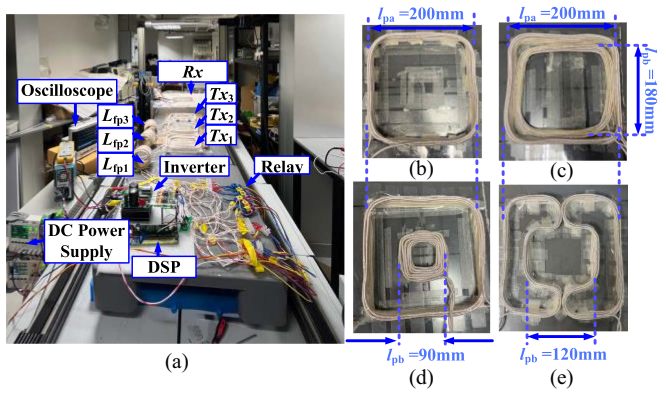

Fig. 15. (a) Photograph of the experimental setup and dimensions of (b) Design-1, (c) Design-2, (d) Design-3, and (e) Design-4 Tx coils.

the compensation coil in Fig. 8(a) (i.e., 1.485 μH). However, the positions of M_{psmax} and M_{psmin} in Fig. 13(b) do not occur at the typical positions shown in Fig. 13(a) (i.e., TD$_{\text{smax}}$ = 250 mm and TD$_{\text{smin}}$ = 375 mm). These extra fluctuations are caused by the presence of Tx*b*. Consequently, the method of using ΔM_{ps} at typical positions to evaluate fluctuations [32] is no longer entirely applicable. Instead, the derivative of M_{passum} with respect to TD$_s$, as described in (13), provides a more robust and universally applicable calculation method, accommodating diverse coil designs and ensuring a reliable evaluation of mutual inductance variations.

Fig. 14 shows the curves of M_{pxas}, M_{pxbs}, and M_{ps} for the proposed design in Fig. 12 with l_{pb} = 120 mm of the DIPT system. It is evident from Fig. 14 that this novel configuration can achieve performance comparable to the IOS Tx coil units, provided that the current directions are appropriately aligned, as depicted in Fig. 12(a). A key advantage of the proposed design is its ability to address interoperability issues with bipolar Rx coils, while IOS Tx coil units in Fig. 9 cannot. The IOS Tx coil units are specifically optimized for unipolar Rx coils (refer to Fig. 6). It cancels the magnetic flux of bipolar Rx coils, such as the typical double-D (DD) coil, resulting in zero-induced voltage at the receiver side. Consequently, it is not applicable to match with bipolar Rx coils. By altering the connection of the THST coils, specifically by reversing the current direction in the right-side coil, the system can adapt to bipolar Rx configurations. This adaptability ensures that the system is compatible with both unipolar and bipolar Rx coils, thereby enhancing its versatility and practical application in DIPT systems.

V. Experimental Verifications

Experiments are performed on the prototype, as shown in Fig. 15(a). Fig. 15(b)–(e) shows the dimensions of the conventional Tx coil without compensation coil, two antiseries connections of IOS coils, and THST coils (i.e., Design-1, Design-2, Design-3, and Design-4). To maintain similar M_{ps} designed by the algorithm in Fig. 10 for the DIPT system, Design-2 was wound with 7 turns, Design-3 with 21 turns, and Design-4 with 10 turns. The corresponding self-inductance L_p for the Tx coil

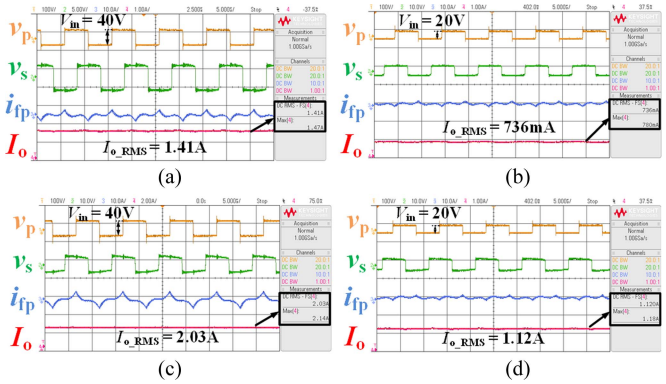

Fig. 16. Waveforms of v_{p}, v_{s}, i_{fp}, and I_{o} of DIPT system with (a) Design-1 at V_{in} = 40 V, (b) Design-1 at V_{in} = 20 V, (c) Design-2 in aiding-series connection at V_{in} = 40 V, and (d) Design-2 in aiding-series connection at V_{in} = 20 V.

with series-opposing connection in Fig. 15 are 43, 30.64, 61.19, and 50.74 μH. The planar spiral square and DD Rx coil with coil dimensions set to l_s = 200 mm, are tightly wound with 12 and 10 turns, respectively. The corresponding self-inductance L_s are 36 μH and 55.57 μH. The nominal coupling coefficients between these design Tx coil and the planar spiral square Rx are 0.21, 0.12, 0.11, and 0.1. The diode-bridge rectifier is composed of SiC Schottky diodes E6D20065A. The digital signal processor TMS320F28335 is employed to generate the switching signal required to drive the primary-side SiC inverter TARAZ SPM-FB. The operating frequency f_s and phase shift angle α are fixed at 100 kHz and 0°, respectively.

A. Performance Evaluation of Design-2 in Aiding-Series Connection

To demonstrate the effectiveness of the IOS reconfigurable Tx coil units in resisting input voltage variations, experiments are conducted on the DIPT system with a planar spiral square Rx coil well aligned with the Tx coil. Fig. 16 shows the comparative waveforms for Tx coils with Design-1 and Design-2 in aiding-series connection at V_{in} = 40 V and V_{in} = 20 V. As a result, the reconfigurable Tx coil exhibits stronger robustness and flexibility. As depicted in Fig. 16(a) and (b), output current *I*

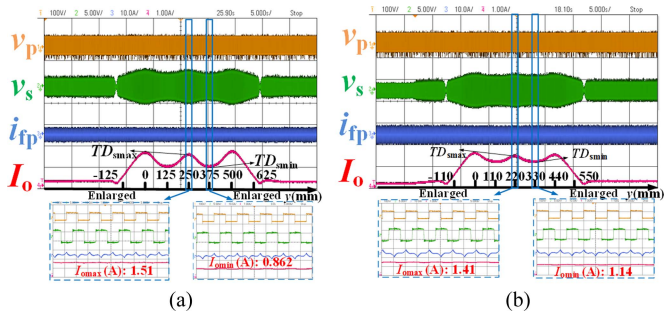

Fig. 17. Waveforms of v_{p}, v_{s}, i_{fp}, and I_{o} of DIPT system (a) with $d_{\mathrm{p12}} = 50$ mm and (b) with $d_{\mathrm{p12}} = 20$ mm.

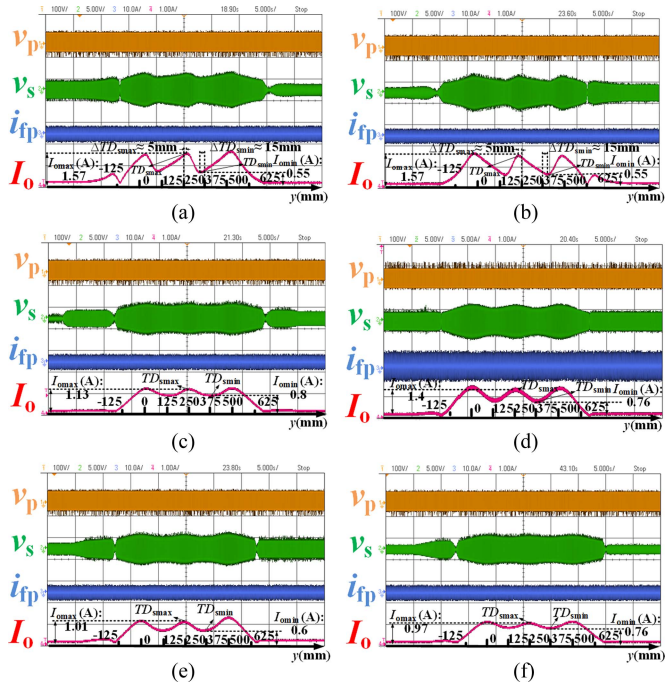

Fig. 18. Waveforms of v_p, v_s, i_{fp}, and I_{o} of DIPT system in (a) scenario-1, (b) scenario-2, (c) scenario-3, (d) scenario-4, (e) scenario-5, and (f) scenario-6.

$_{\mathrm{o}}$ changes from 1.41 to 0.736 A with voltage changing from 40 to 20 V, while for the Tx coil with Design-2 in aiding-series connection, it changes from 2.03 to 1.12 A, as shown in Fig. 16(c) and (d). By incorporating a compensation coil with an aiding-series connection under low voltage conditions, the back-end dc–dc converter can be operated within the controllable range [14] and the system exhibits an enhanced output range.

B. Effects of Separation Between Adjacent Tx Coils and Misalignments on Output Fluctuation

To evaluate the impact of the separation distance (d_{p12}) between adjacent Tx coils on the output current (I_{o}), comparisons of $d_{\mathrm{p12}} = 50$ mm and $d_{\mathrm{p12}} = 20$ mm based on Design-1 are given on the DIPT system with $V_{\mathrm{in}} = 40$ V and $R_L = 1\ \Omega$. Fig. 17 illustrates the waveforms of v_p, v_s, i_{fp}, and I_{o} for the conventional DIPT system without a compensation Tx coil when the Rx moves along the y-axis. According to (4), the maximum (I_{omax}) and minimum values of I_{o} (I_{omin}) correspond to M_{pasmax} and M_{pasmin} are observed during Rx movement. Apparently, the I_{omax} and I_{omin} occur at typical positions, i.e., Rx is directly above the center of the Tx coil and directly above the center of the separation gap. The fluctuation of I_{o} is more pronounced with a larger d_{p12}. Besides, the reduction of I_{omin} is 24.38%, while I_{omax} increases by 7% with a larger d_{p12}, indicating that the impact of d_{p12} is more significant than the cross-coupling impact.

To validate the analysis that misalignments of Rx can affect the position of $\mathrm{TD_{smax}}$ and $\mathrm{TD_{smin}}$, six scenarios of Rx movement with various misalignments are tested.

1) Scenario-1: Angular misalignments with $\theta_{\mathrm{x}} = 30^{\circ}$
2) Scenario-2: Angular misalignments with $\theta_{\mathrm{x}} = -30^{\circ}$
3) Scenario-3: Angular misalignments with $\theta_{\mathrm{y}} = 30^{\circ}$
4) Scenario-4: Angular misalignments with $\theta_{\mathrm{z}} = 30^{\circ}$
5) Scenario-5: Linear misalignments with $x_{\mathrm{lm}} = 60$ mm
6) Scenario-6: Linear misalignments with $z_{\mathrm{lm}} = 30$ mm

Fig. 18 shows the waveforms of v_p, v_s, i_{fp}, and I_{o} for all scenarios. For Scenario-3, Scenario-4, Scenario-5, and Scenario-6, I_{omax} and I_{omin} occur at typical positions. However, in Scenario-1 and Scenario-2, offsets in $\mathrm{TD_{smax}}$ and $\mathrm{TD_{smin}}$ are observed. Compared to the typical positions (i.e., $\mathrm{TD_{smax}} = 250$ mm and $\mathrm{TD_{smin}} = 375$ mm), $\mathrm{TD_{smin}}$ shifts from 375 to 360 mm, while $\mathrm{TD_{smax}}$ shifts from 250 to 255 mm in Scenario-1. $\mathrm{TD_{smax}}$ and $\mathrm{TD_{smin}}$ in Scenario-2 have the opposite offset to Scenario-1. Therefore, the conventional design reference at the fixed positions [32] does not apply to the system with θ_x misalignments. Moreover, Rx with angular misalignments around the x-axis exhibits the largest effect on the output current fluctuation at 65.8% among all scenarios, notably larger than the fluctuation without misalignments (42.9%), as illustrated in Fig. 17(a). This phenomenon arises θ_x intensifies the unevenness of mutual inductance along the y-axis. Other misalignments weaken the fluctuation phenomenon.

C. Output Fluctuation Suppression Performance

To exhibit superior output fluctuation suppression performance of the proposed reconfigurable Tx coils with antiseries connection shown in Fig. 15(c)–(e) over conventional Tx coils (i.e., Design-1), experiments are carried out based on the DIPT system with $V_{\mathrm{in}} = 40$ V and $R_L = 1\ \Omega$. The corresponding waveforms of v_p, v_s, i_{fp}, and I_{o} with proposed Tx coils are shown in Fig. 19. Obviously, the suppression fluctuation performance of the proposed Design-2, Design-3, and Design-4 Tx coils with series-opposing connections is significantly improved compared to the conventional counterparts in Fig. 17(a). The output current fluctuation ΔI_{o} in Fig. 19 is reduced from 0.89 to 0.14 A, 0.148 A, and 0.08 A, respectively. Although the reduction of I_{omax} is 50.9%, 44.5%, and 54.3%, they are close to the minimum value in Fig. 17(a). The calculated l_{pb}, n_{pbk}, and n_{pbki} are close to the real l_{pb}, n_{pbk}, and n_{pbki}, which proves the effectiveness of the proposed algorithm in Fig. 10. Besides, both I_{o} with Design-3 and Design-4 Tx coils exhibit extra fluctuation, indicating that the previously observed typical position of I

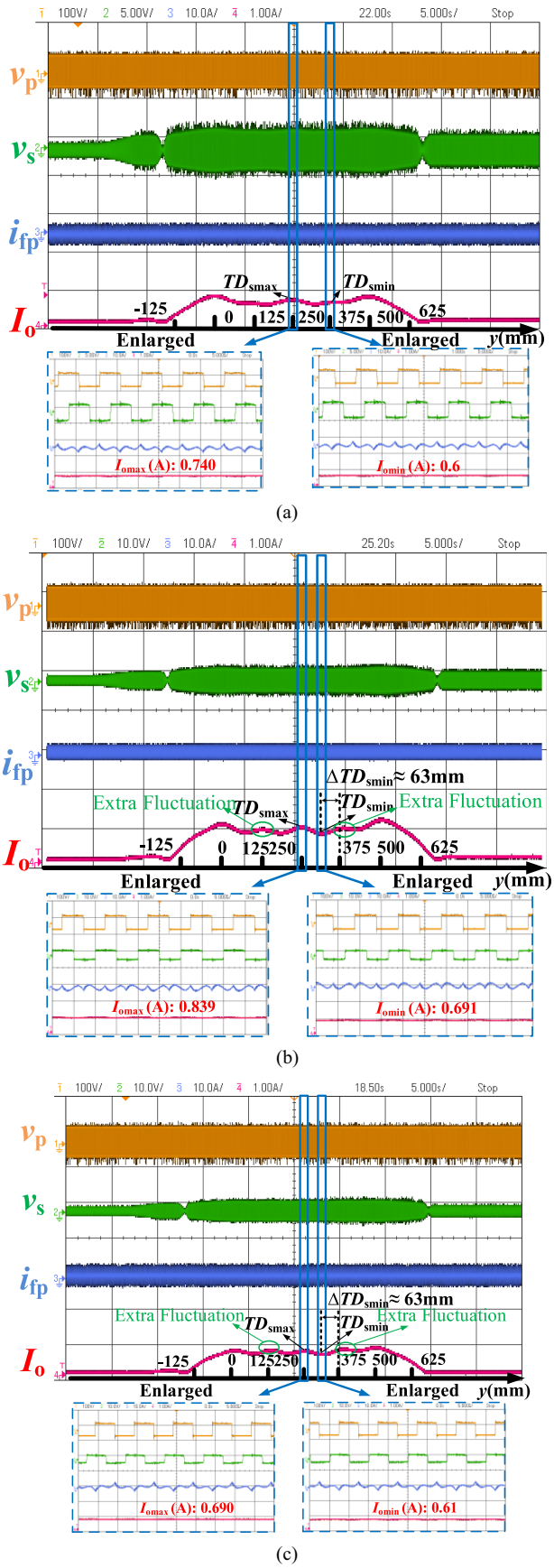

Fig. 19. Waveforms of v_p, v_s, i_{fp}, and I_o of DIPT system with (a) Design-2, (b) Design-3, and (c) Design-4 Tx coils in series-opposing connection.

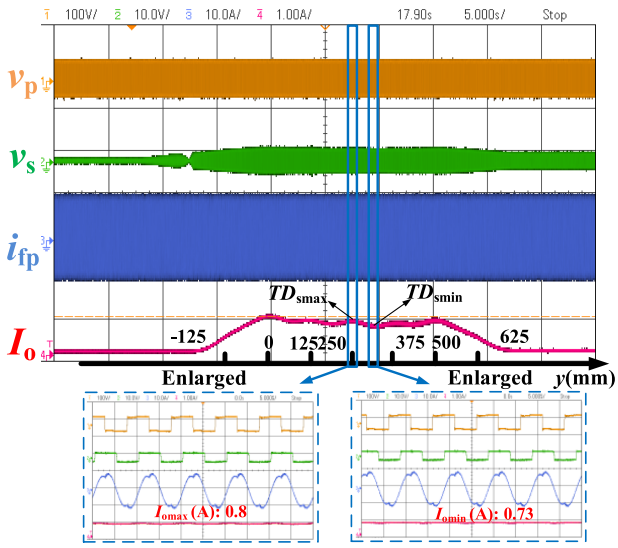

Fig. 20. Waveforms of v_p, v_s, i_{fp}, and I_o of the DIPT system with Design-4 Tx coils in aiding-series connection matching with the DD Rx coil.

$_{omin}$ (TD_{smin}) shifts. Overcompensation of the reverse coil may even cause this position to the maximum value. Therefore, the conventional design reference at the fixed positions [32] does not apply to the system with overcompensation coils.

D. Interoperability Performance of THST Tx Coils

To further validate the generality of the proposed THST Tx coils (i.e., Design-4) with aiding-series connection matching with bipolar Rx coils, experiments are also conducted on the DIPT system with $V_{in} = 40$ V, $R_L = 1\ \Omega$. The corresponding waveforms of v_p, v_s, i_{fp}, and I_o are shown in Fig. 20. Obviously, the results in Figs. 19(c) and 20 verify that the proposed Design-4 is suitable for bipolar and unipolar Rx coils and reduces fluctuation.

E. Power Loss Analysis

The system power losses for the proposed designs [see Fig. 15(b)–(e)] are measured at their maximum efficiency points, as illustrated in Fig. 21. The recorded power losses are 6.4, 11.877, 9.237, and 8.18 W, with corresponding maximum dc–dc efficiencies of 86.1%, 84.1%, 84.6%, and 82.7%, respectively. Coils and compensation structures account for 50% –60% of total system losses, primarily due to the absence of high magnetic permeability materials (e.g., ferrites) to guide flux and the elevated ESR of extended transmission lines and components. Power electronics (inverters/rectifiers) contribute 40% of losses, including switching, conduction, and gate driver losses. To address these inefficiencies, a modular integrated design will be proposed in future work to minimize parasitic parameters and reduce ESR across the system. Systems incorporating the compensation coil (Fig. 15(c), (d), and (e)) exhibit slightly lower efficiency compared to the system without the compensation coil [see Fig. 15(b)], primarily due to the power dissipation introduced by the integrated relay and compensation coil. Despite this

TABLE II
COMPARISON OF THE EXISTING DIPT SYSTEM

Reference	Tx and Rx structure	Tx excitation conditions	Separation distance/ Tx side length	Output variation	Mutual inductance reduction	Copper cost	With & without Ferrite	Reconfigurability	Interoperability
[8]	Interdigitated DD+Rec and DDQ	N/A	zero	≤2%	×	High	√	×	**Average**
[9]	Rec and Rec	N/A	zero	≤2.5%	×	Moderate	×	×	**Area for growth**
[16]	Folded Rec and Rec	N/A	zero	0%	×	Moderate	√	×	**Area for growth**
[18]	Rec+SP and Rec	Phase shift by π/2	50%	≤5.4%	×	Moderate	√	×	**Area for growth**
[28]	Rec+Rev and Rec+Rev	Out of phase	3.3%	≤4%	√	Moderate	√	×	**Area for growth**
[33]	DDQ and DD or Cir	Phase shift by π/2	-33%	≤10%	×	High	√	×	**Good**
[34]	SP and Two-phase DD	Phase shift by π/2	9%	≤32.5%	×	High	√	×	**Area for growth**
This work	IOS and DD or Rec	In or out of phase	25%	≤10%	√	Moderate	×	√	**Area for growth**
This work	THST &and DD or Rec	In or out of phase	25%	≤6%	√	Moderate	×	√	**Good**

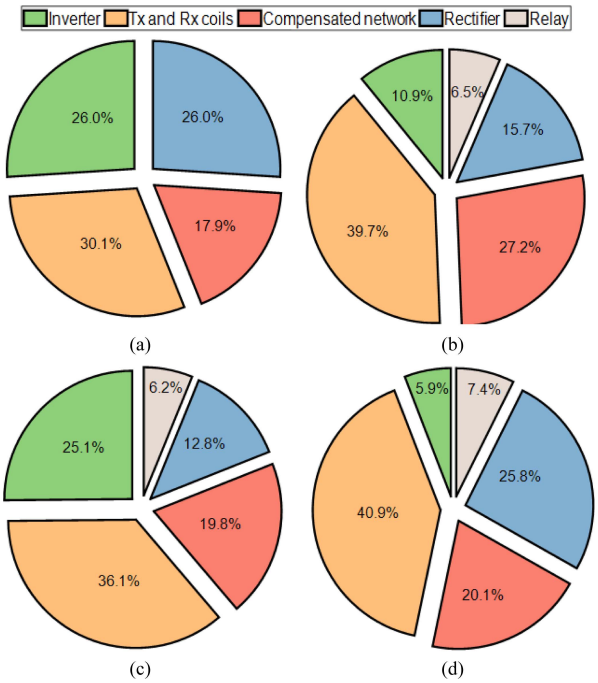

Fig. 21. Power loss distribution of the DIPT system with (a) Design-1 (b) Design-2 (c) Design-3, and (d) Design-4 Tx coils.

localized efficiency reduction, integrating a compensation coil ensures stable input power and consistent output power delivery throughout the receiver's motion, thereby enhancing the overall system robustness. In addition, flexible coil configurations enable a wider output range or enhanced interoperability between unipolar and bipolar Tx coils, effectively accommodating diverse operational requirements.

VI. COMPARISON WITH THE EXISTING DIPT SYSTEMS

Table II compares the key features across the existing DIPT systems. Conventional rectangular Tx coils solve cross-coupling issues without spacing between the adjacent Tx coils by optimally designing the compensated network [9], [16]. Complicated Rx structures must be compatible with the interdigitated unipolar and bipolar Tx [8], as well as the solenoid pad (SP) [34] to smooth the mutual inductance, which increases both copper cost and complexity on the receiver side. Orthogonal SP and rectangular Tx coil configurations [18] and rectangular with reverse Tx structure [28] operate under a constant excitation mode, limiting their adaptability to diverse application scenarios. The alternately arranged DD and Quadrate (DDQ) in [33] exhibit overlapping regions, which not only increase the copper usage, but also necessitate a specific phase shift angle for proper excitation. In this work, the IOS and THST coils with antiseries connections exhibit low coupling variation and stable power output, while minimizing copper usage through reduced Tx coverage density. In addition, when integrated with a switch array, the proposed Tx coils leverage their reconfigurability to enable wide-range operation and interoperability with diverse pickup coil types, enhancing system versatility. It is worth noting that a fair comparison among these methods is challenging, as the table data are derived directly from the cited literature rather than from a standardized benchmark system.

VII. CONCLUSION

This article introduces two novel reconfigurable array-type Tx coil designs: IOS Tx coil units, and THST Tx coil units. These designs aim to enhance the performance of DIPT systems. Both simulation and experimental results validate that the antiseries connections of these coil units significantly suppress output fluctuations compared to conventional single Tx coil units. When integrated with a switch array for reconfiguring the connections of coil sets, the IOS and THST Tx coil units exhibit distinct inherent advantages. Specifically, the IOS Tx coil units provide a wider output range, while the THST Tx coil units offer enhanced interoperability with unipolar and bipolar Rx coils. Furthermore, this article proposes a numerical approach for designing main and compensated Tx coil sets and evaluating the impact of linear and angular misalignments on the shift

positions of maximum and minimum mutual inductance, as well as on output fluctuations. Overall, the reconfigurable Tx coils presented in this article not only provide a robust solution for mitigating output variation effects in DIPT systems but also pave the way for future advancements in coil design, ensuring more reliable and flexible wireless power transfer.

REFERENCES

[1] C. T. Rim and C. Mi, *Wireless Power Transfer for Electric Vehicles and Mobile Devices*. Hoboken, NJ, USA: Wiley, 2017.

[2] G. R. Nagendra, G. A. Covic, and J. T. Boys, "Sizing of inductive power pads for dynamic charging of EVs on IPT highways," *IEEE Trans. Transp. Electrific.*, vol. 3, no. 2, pp. 405–417, Jun. 2017.

[3] J. P. K. Sampath, D. M. Vilathgamuwa, and A. Alphones, "Efficiency enhancement for dynamic wireless power transfer system with segmented transmitter array," *IEEE Trans. Transp. Electrific.*, vol. 2, no. 1, pp. 76–85, Mar. 2016.

[4] R. Tavakoli, E. M. Dede, C. Chou, and Z. Pantic, "Cost-efficiency optimization of ground assemblies for dynamic wireless charging of electric vehicles," *IEEE Trans. Transp. Electrific.*, vol. 8, no. 1, pp. 734–751, Mar. 2022.

[5] A. Zaheer, H. Hao, G. A. Covic, and D. Kacprzak, "Investigation of multiple decoupled coil primary pad topologies in lumped IPT systems for interoperable electric vehicle charging," *IEEE Trans. Power Electron.*, vol. 30, no. 4, pp. 1937–1955, Apr. 2015.

[6] T. Fujita, T. Yasuda, and H. Akagi, "A dynamic wireless power transfer system applicable to a stationary system," *IEEE Trans. Ind. Appl.*, vol. 53, no. 4, pp. 3748–3757, Jul./Aug. 2017.

[7] J. M. Miller et al., "Demonstrating dynamic wireless charging of an electric vehicle: The benefit of electrochemical capacitor smoothing," *IEEE Power Electron. Mag.*, vol. 1, no. 1, pp. 12–24, Mar. 2014.

[8] Y. Li et al., "A new coil structure and its optimization design with constant output voltage and constant output current for electric vehicle dynamic wireless charging," *IEEE Trans. Ind. Informat.*, vol. 15, no. 9, pp. 5244–5256, Sep. 2019.

[9] X. Li, J. Hu, H. Wang, X. Dai, and Y. Sun, "A new coupling structure and position detection method for segmented control dynamic wireless power transfer systems," *IEEE Trans. Power Electron.*, vol. 35, no. 7, pp. 6741–6745, Jul. 2020.

[10] K. Kumar, K. V. V. S. R. Chowdary, P. Sanjeevikumar, and R. Prasad, "Analysis of solar PV fed dynamic wireless charging system for electric vehicles," in *Proc. IEEE 47th Annu. Conf. Ind. Electron. Soc.*, 2021, pp. 1–6.

[11] Y. Yao, Y. Wang, X. Liu, K. Lu, and D. Xu, "Analysis and design of an S/SP compensated IPT system to minimize output voltage fluctuation versus coupling coefficient and load variation," *IEEE Trans. Veh. Technol.*, vol. 67, no. 10, pp. 9262–9272, Oct. 2018.

[12] S. Kim, G. A. Covic, and J. T. Boys, "Comparison of tripolar and circular pads for IPT charging systems," *IEEE Trans. Power Electron.*, vol. 33, no. 7, pp. 6093–6103, Jul. 2018.

[13] H. Xiao, Y. Yang, K. Wang, and J. Wu, "Comparative studies of front-end model predictive control for direct inductive power transfer systems," *IEEE Trans. Power Electron.*, vol. 38, no. 10, pp. 11885–11897, Oct. 2023.

[14] T. Tan, K. Chen, Q. Lin, Y. Jiang, L. Yuan, and Z. Zhao, "Impedance shaping control strategy for wireless power transfer system based on dynamic small-signal analysis," *IEEE Trans. Circuits Syst. I, Reg. Papers*, vol. 68, no. 3, pp. 1354–1365, Mar. 2021.

[15] J. Choi, J. Xu, R. Makhoul, and J. M. R. Davila, "Implementing an impedance compression network to compensate for misalignments in a wireless power transfer system," *IEEE Trans. Power Electron.*, vol. 34, no. 5, pp. 4173–4184, May 2019.

[16] E. S. Lee, M. Y. Kim, S. M. Kang, and S. H. Han, "Segmented IPT coil design for continuous multiple charging of an electrified monorail system," *IEEE Trans. Power Electron.*, vol. 37, no. 3, pp. 3636–3649, Mar. 2022.

[17] E. S. Lee, D. Kim, and S. Y. Jeong, "Triangular DQ Tx coils of wireless EV chargers for large misalignment tolerances," *IEEE Trans. Veh. Technol.*, vol. 72, no. 11, pp. 14179–14188, Nov. 2023.

[18] H. Xu and Z. Huang, "Alternately arranged segmented transmitter pads with magnetic field complementation for suppressing power fluctuation in dynamic wireless power transfer," *IEEE Trans. Power Electron.*, vol. 39, no. 10, pp. 14091–14102, Oct. 2024.

[19] H. Li, Y. Liu, K. Zhou, Z. He, W. Li, and R. Mai, "Uniform power IPT system with three-phase transmitter and bipolar receiver for dynamic charging," *IEEE Trans. Power Electron.*, vol. 34, no. 3, pp. 2013–2017, Mar. 2019.

[20] Y. Geng, Q. Guo, Z. Yang, F. Lin, and Y. Wang, "Design and optimization of real-time strong coupling coil of dynamic wireless power transfer for electrical vehicle," *IEEE Trans. Veh. Technol.*, vol. 72, no. 9, pp. 11495–11504, Sep. 2023.

[21] C. Cai, M. Saeedifard, J. Wang, P. Zhang, J. Zhao, and Y. Hong, "A cost-effective segmented dynamic wireless charging system with stable efficiency and output power," *IEEE Trans. Power Electron.*, vol. 37, no. 7, pp. 8682–8700, Jul. 2022.

[22] Y. Liu, R. Mai, D. Liu, Y. Li, and Z. He, "Efficiency optimization for wireless dynamic charging system with overlapped DD coil arrays," *IEEE Trans. Power Electron.*, vol. 33, no. 4, pp. 2832–2846, Apr. 2018.

[23] J. Yin, S. Mekhilef, P. Darvish, H. Mokhlis, and T. K. Soon, "A new cross-overlapped decoupling coil structure for EV dynamic inductive wireless charging system," *IEEE Trans. Ind. Electron.*, vol. 72, no. 2, pp. 1314–1324, Feb. 2025.

[24] W.-S. Lee, W.-I. Son, K.-S. Oh, and J.-W. Yu, "Contactless energy transfer systems using antiparallel resonant loops," *IEEE Trans. Ind. Electron.*, vol. 60, no. 1, pp. 350–359, Jan. 2013.

[25] Y. Zhang, S. Chen, X. Li, and Y. Tang, "Design methodology of free-positioning nonoverlapping wireless charging for consumer electronics based on antiparallel windings," *IEEE Trans. Ind. Electron.*, vol. 69, no. 1, pp. 825–834, Jan. 2022.

[26] Z. Dong, X. Li, S. Liu, Z. Xu, and L. Yang, "A novel all-direction antimisalignment wireless power transfer system designed by truncated region eigenfunction expansion method," *IEEE Trans. Power Electron.*, vol. 36, no. 11, pp. 12456–12467, Nov. 2021.

[27] W.-S. Lee, K.-S. Oh, and J.-W. Yu, "Field analysis and measurement of antiparallel resonant loop for wireless charging," *IEEE Antennas Wireless Propag. Lett.*, vol. 14, pp. 1459–1462, 2015.

[28] K. Shi, C. Tang, Z. Wang, X. Li, Y. Zhou, and Y. Fei, "A magnetic integrated method suppressing power fluctuation for EV dynamic wireless charging system," *IEEE Trans. Power Electron.*, vol. 37, no. 6, pp. 7493–7503, Jun. 2022.

[29] Y. Yang, "Precise Modeling of Nonlinear Rectifier Loads in Wireless Power Transfer Systems," *IEEE J. Emerg. Sel. Top. Power Electron.*, vol. 11, no. 3, pp. 3574–3585, Jun. 2023.

[30] T. Theodoropoulos et al., "Impact of dynamic EV wireless charging on the grid," in *Proc. IEEE Int. Electric Veh. Conf.*, 2014, pp. 1–7.

[31] A. O. Mirzaei, M. Asadi, H. Ghanbarpour, A. M. Abazari, and H. Tavakkoli, "Mutual inductance calculations of non-identical n-sided planar coils with arbitrary geometry and spatial orientations," *Eur. Phys. J. Plus*, vol. 138, no. 9, Sep. 2023, Art. no. 869.

[32] K. Shi, C. Tang, H. Long, X. Lv, Z. Wang, and X. Li, "Power fluctuation suppression method for EV dynamic wireless charging system based on integrated magnetic coupler," *IEEE Trans. Power Electron.*, vol. 37, no. 1, pp. 1118–1131, Jan. 2022.

[33] W. Chen, F. Lin, and G. A. Covic, "A modified DDQ track for interoperable EV dynamic charging," *IEEE Trans. Power Electron.*, vol. 38, no. 10, pp. 11738–11750, Oct. 2023.

[34] F. Zhao, S. Cui, C. C. Chan, and C. Zhu, "Modeling of high-efficiency nonsalient pole transmitter in high-power dynamic wireless charging system for electric vehicles," *IEEE Trans. Power Electron.*, vol. 39, no. 7, pp. 8872–8882, Jul. 2024.

Huiwen Xiao (Graduate Student Member, IEEE) received the B.Sc. degree in electrical engineering and automation from Hebei University of Technology, Tianjin, China, in 2017, and M.Eng. degree in electrical engineering from the University of Chinese Academy of Sciences, Beijing, China, in 2020. She is currently working toward the Ph.D. degree in power electronics with the Department of Electrical and Electronic Engineering, Faculty of Engineering, Hong Kong Polytechnic University, Hong Kong.

Before joining the Hong Kong Polytechnic University, she was with the Institute of Electrical Engineering, Chinese Academy of Sciences as an Engineer. Her current research interests include inductive/wireless power transfer and electric vehicles.

Ka Wai Eric Cheng (Fellow, IEEE) received the B.Sc. degree in electrical and electronic engineering and the Ph.D. degree in power electronics from the University of Bath, Bath, U.K., in 1987 and 1990, respectively.

Before joining The Hong Kong Polytechnic University, Hong Kong, in 1997, he was with Lucas Aerospace, London, U.K., as a Principal Engineer. He is currently a Professor of Electrical Engineering, School of Engineering, The University of California, Merced, CA, USA. He has authored or coauthored more than 500 articles and seven books. His research interests include all aspects of power electronics, motor drives, electromagnetic interference, electric vehicles, battery management, and energy saving.

Dr. Cheng was a recipient of the Institution of Electrical Engineers Sebastian Z De Ferranti Premium Award, in 1995; the Outstanding Consultancy Award, in 2000; the Faculty Merit Award for Best Teaching from The Hong Kong Polytechnic University, in 2003; the Faculty Engineering Industrial and Engineering Services Grant Achievement Award, in 2006; the Brussels Innova Energy Gold Medal with Mention, in 2007; the Consumer Product Design Award, in 2008; the Electric Vehicle Team Merit Award of the Faculty, in 2009; the Eco Star Award, in 2012; the Gold Prize Seoul International Invention Fair, in 2015; the iCAN Gold Medal at Canada for contribution in active suspension, in 2016; the Gold Award of HK Innovation and Technology for contribution in body integrated supercapacitor for vehicles, in 2017, the Geneva Invention Expo Silver Medal for contribution in e-Antilock braking systems, in 2021, and TechConnect 2023 and Geneva Invention 2024 for the contribution in Ammonia Electric Vehicles.

Siqi Bu (Senior Member, IEEE) received the Ph.D. degree in power systems from the Electric Power and Energy Research Cluster, The Queen's University of Belfast, Belfast, U.K., in 2012.

In Electric Power and Energy Research Cluster, The Queen's University of Belfast, he continued his postdoctoral research work before entering industry. Then, he was with National Grid U.K. as an experienced U.K. National Transmission System Planner and Operator. He is currently a Professor and Associate Head with the Department of Electrical and Electronic Engineering, The Hong Kong Polytechnic University, Kowloon, Hong Kong, Associate Director of Research Centre for Grid Modernisation, and a Chartered Engineer with the U.K. Royal Engineering Council, London, U.K. His research interests include power system stability, operation and economics considering renewable energy integration, smart grid application, and transport electrification.

Dr. Bu is an Editor of IEEE TRANSACTIONS ON POWER SYSTEMS, IEEE TRANSACTIONS ON CONSUMER ELECTRONICS, IEEE POWER ENGINEERING LETTERS, IEEE OPEN ACCESS JOURNAL OF POWER AND ENERGY, *CSEE Journal of Power and Energy Systems*, *Protection and Control of Modern Power Systems*, *Journal of Modern Power Systems and Clean Energy*, and *Advances in Applied Energy*. He is a Fellow of IET, Chair of IET HK Power and Energy Section, Cochair of IET DPSP 2025 and APSCOM 2025, and Technical Chair of IEEE PESIM 2026.